MRI estimates of brain iron concentration in normal aging: Comparison of field-dependent (FDRI) and phase (SWI) methods

Citation: Pfefferbaum, Adolf, Elfar Adalsteinsson, Torsten Rohlfing, and Edith V. Sullivan. "MRI Estimates of Brain Iron Concentration in Normal Aging: Comparison of Field-Dependent (FDRI) and Phase (SWI) Methods." NeuroImage 47, no. 2 (August 2009): 493–500.

As Published: http://dx.doi.org/10.1016/j.neuroimage.2009.05.006

Publisher: Elsevier

Persistent URL: http://hdl.handle.net/1721.1/99702

Version: Author's final manuscript: final author's manuscript post peer review, without publisher's formatting or copy editing

Published in final edited form as:
Neuroimage. 2009 August 15; 47(2): 493–500. doi:10.1016/j.neuroimage.2009.05.006.

MRI Estimates of Brain Iron Concentration in Normal Aging: Comparison of Field-Dependent (FDRI) and Phase (SWI) Methods

Adolf Pfefferbaum[1,2], **Elfar Adalsteinsson**[3,4], **Torsten Rohlfing**[1], and **Edith V. Sullivan**[2]

[1]Neuroscience Program, SRI International

[2]Department of Psychiatry and Behavioral Sciences, Stanford University School of Medicine

[3]Department of Electrical Engineering and Computer Science, Massachusetts Institute of Technology

[4]Harvard-MIT Division of Health Sciences & Technology, Massachusetts Institute of Technology

Abstract

Different brain structures accumulate iron at different rates throughout the adult life span. Typically, striatal and brain stem structures are higher in iron concentrations in older than younger adults, whereas cortical white matter and thalamus have lower concentrations in the elderly than young adults. Brain iron can be measured in vivo with MRI by estimating the relaxivity increase across magnetic field strengths, which yields the Field-Dependent R2 Increase (FDRI) metric. The influence of local iron deposition on susceptibility, manifest as MR phase effects, forms the basis for another approach for iron measurement, Susceptibility-Weighted Imaging (SWI), for which imaging at only one field strength is sufficient. Here, we compared the ability of these two methods to detect and quantify brain iron in 11 young (5 men, 6 women; 21 to 29 years) and 12 elderly (6 men, 6 women; 64 to 86 years) healthy adults. FDRI was acquired at 1.5T and 3.0T, and SWI was acquired at 1.5T. The results showed that both methods detected high globus pallidus iron concentration regardless of age and significantly greater iron in putamen with advancing age. The SWI measures were more sensitive when the phase signal intensities themselves were used to define regions of interest, whereas FDRI measures were robust to the method of region of interest selection. Further, FDRI measures were more highly correlated than SWI iron estimates with published postmortem values and were more sensitive than SWI to iron concentration differences across basal ganglia structures. Whereas FDRI requires more imaging time than SWI, two field strengths, and across-study image registration for iron concentration calculation, FDRI appears more specific to age-dependent accumulation of non-heme brain iron than SWI, which is affected by heme iron and non-iron source effects on phase.

Introduction

Convergent postmortem (Hallgren and Sourander, 1958) and in vivo data indicate that deep gray matter brain structures accumulate ferritin at different rates throughout adult aging (Bartzokis et al., 1994; Bartzokis et al., 2007b; Bizzi et al., 1990). The structures affected support motor functioning, and increasing iron deposition may contribute to age-related motor slowing. Abnormal iron accumulation has been reported in neurological conditions involving the striatum, including Parkinson's disease, multiple sclerosis, substantia nigra degeneration, multisystems atrophy, Huntington's disease, and Hallervorden-Spatz syndrome (reviewed in Bartzokis et al., 2007a; Bartzokis et al., 2007b; Brass et al., 2006; Haacke et al., 2005; Haacke

Correspondence: Edith V. Sullivan, Ph.D. Stanford University School of Medicine Department of Psychiatry and Behavioral Sciences 401 Quarry Road Stanford, CA 94305-5723 650-498-7328 (phone) 650-859-2743 (FAX) edie@stanford.edu.

et al., 2009; Mittal et al., 2009), and suggests that iron burden contributes to age- and disease-related functional decline (Bartzokis et al., 2008; Sullivan et al., 2009).

Iron can be measured in vivo with MR imaging because of iron's effect on signal intensity, causing signal darkening on T2* and T2-weighted images that is greater with increasing magnetic field strength. By estimating the transverse relaxivity increase across field strengths, the MR Field Dependent Relaxivity Increase (FDRI) can be calculated (Bartzokis et al., 1993; Bartzokis et al., 2007b; Pfefferbaum et al., 2009). For example, acquisition of spin-echo data with a constant TR and multiple echoes at 1.5T and 3.0T allows the computation of R2 at each field strength, with the difference between R2s divided by the field strength difference producing FDRI in units of s^{-1}/Tesla.

In addition to affecting relaxivity, local iron influences MR gradient-echo image phase, which forms the basis for another method for iron quantification, Susceptibility-Weighted Imaging (SWI) (Haacke et al., 2005; Haacke et al., 2004). The paramagnetic properties of tissue ferritin cause local field inhomogeneity that can be detected by examining the phase of the spins computed from the relationship of the real and imaginary components of quadrature-detected signal in a gradient-echo sequence. The phase of the spins at a given field strength and echo time are influenced by iron concentration in each voxel. The ferromagnetic property of the iron causes the protons to accrue more negative phase in iron-rich tissue in addition to off-resonance phase accrued linearly with field strength and echo time. For a right-handed system, reconstructed MR phase images typically yield positive phase values for white matter (less iron), whereas deep gray matter structures tend to have negative phase (more iron). In addition to iron content, the phase of the spins in a voxel can also be influenced by other sources, including main-field inhomogeneities due to air-tissue interfaces, flowing or moving spins, and the ratio of oxy- and dexoyhemoglobin. At optimal acquisition parameters, the more iron in a voxel, the lower will be the measured phase (Haacke et al., 2004). An advantage of this approach is that it does not require scanning at two field strengths (Haacke et al., 2007; Haacke et al., 2005).

We compared the FDRI and SWI approaches to measurement of brain iron in regions known to vary widely in their iron content—high in striatum and brain stem nuclei and low in white matter—and affected differentially by age. To establish convergent validity of the results, we correlated the regional iron values obtained with each acquisition method with published postmortem values on regional brain iron (Hallgren and Sourander, 1958).

Methods

Subjects

Two groups of healthy, highly educated, right-handed adults were studied: 11 younger (mean=24.0±2.5, range=21 to 29 years, 15.9 years of education; 5 men, 6 women) and 12 older (mean=74.4±7.6, range=64 to 86 years, 16.3 years of education; 6 men, 6 women). The younger subjects included laboratory members and volunteers recruited from the local community. All older participants were recruited from a larger ongoing study of normal aging and scored well within the normal range on the Dementia Rating Scale (Mattis, 1988): mean=140.6, range=132 to 144 out of 144, cutoff for dementia=124. Mean (and range) of days between 1.5T and 3.0T scan acquisition were 16.5 (0 to 56) days for the young and 9.3 (0 to 42) days for the elderly group; for 2 of the young and 8 of the elderly all scans were acquired on the same day.

Image Acquisition Protocols

MRI data were acquired prospectively on 1.5T and 3.0T General Electric (Milwaukee, WI) Signa human MRI scanners (gradient strength=40mT/m; slew rate=150 T/m/s). In keeping

with reports of Haacke and colleagues and in an effort to replicate published methods, we collected SWI data at 1.5T (Haacke et al., 2009; Haacke et al., 2004; Ogg et al., 1999).

FDRI acquisition—At 1.5T, after autoshimming for the session, the following sequences were acquired for 62 axial slices, each 2.5-mm thick: 1) 3D SPoiled Gradient Recalled Echo (SPGR) for structural imaging and registration (TR/TE=8.1/3.3 ms, FA=30 degrees); 2) Multi-shot Echo Planar Spin Echo (EPSE) (TR/TE 6000/17, FA=90 degrees, 256×192 inplane, FOV=24 cm, 4 NEX, 24 interleaves with 8 phase-encode lines per TR, 9:40 min); 3) Multi-shot EPSE (TR/TE 6000/60, FA=90 degrees, 256×192 inplane, FOV=24 cm, 6 NEX, 24 interleaves, 14:20 min).

At 3.0T, after autoshimming for the session, the following sequences were acquired in the axial plane: 1) 3D SPGR for structural imaging and registration (TR/TE=8.1/3.3 ms, FA=15 degrees, 124 slices, 1.25mm thick) 2) Multi-shot EPSE (TR/TE 6000/17, FA=90 degrees, 256×192 inplane, FOV=24 cm, 3 NEX, 24 interleaves, 62 slices, 2.5mm thick, 7:10 min); 3) Multi-shot EPSE (TR/TE 6000/60 ms, FA=90 degrees, 256×192 inplane, FOV=24 cm, 6 NEX, 24 interleaves, 62 slices, 2.5mm thick, 14:20 min).

SWI acquisition—At 1.5T, after autoshimming for the session, the following sequences were acquired for 62 axial slices, each 2.5-mm thick: 1) 3D SPGR for structural imaging and registration (TR/TE=28/10 ms, FA=30 degrees, 256×256 inplane, 24cm FOV); 2) Susceptibility-weighted 3D SPGR (TR/TE=58ms/40ms, FA=15 degrees, 512×256 inplane, 24cm FOV, 12:20 min, with flow compensation (Haacke et al., 2007; Haacke et al., 2005); 3) 2D gradient-recalled echo sequence (TR/TE=600/3ms, FA=20 degrees); 4) 2D gradient-recalled echo sequence (TR/TE=600/7ms, FA=20 degrees).

Phase images were constructed from the real and imaginary components of the SWI SPGR data after the phase was unwrapped with PRELUDE [Phase Region Expanding Labeller for Unwrapping Discrete Estimates (Jenkinson, 2003)]. The magnitude and phase-unwrapped SWI data were down-sampled from 512×256 to 256×256 via averaging to match the FDRI resolution. The complex-valued SWI data (magnitude and unwrapped phase) were then high-pass filtered as described by Wang et al. (Wang et al., 2000) and Haacke et al. (Haacke et al., 2007): a 3D low-pass Hanning filter multiplied the SWI data in k-space and the complex-valued SWI data were then complex divided by the low-pass version in the image domain. The phase of the resulting complex-valued images was used for subsequent analysis. The data were analyzed with Hanning filter of both 64- and 96–pixel extent as recommended by Haacke et al. (Haacke et al., 2007).

Image registration

For each subject, and for 1.5T and 3.0T separately, the late-echo EPSE data were nonrigidly registered (Rohlfing and Maurer, 2003) to the early-echo EPSE data. This was necessary because the two echoes arose from separate acquisitions, rather than a single dual-echo acquisition, and were, therefore, not always perfectly aligned with each other. The 1.5T early-echo EPSE image of each subject was registered to the 3.0T early-echo EPSE image of the same subject, which was then registered nonrigidly to the subject's 3.0T SPGR image. The 3.0T SPGR image from each subject finally was registered nonrigidly to the SPGR channel of the SRI24 atlas (Rohlfing et al., 2008). Via concatenation of the aforementioned registration transformations, the 1.5T and 3.0T early-echo and late-echo images were all reformatted into 1-mm isotropic SRI24 space, each using a single interpolation with a 5-pixel radius cosine-windowed sinc kernel. Reformatting both 1.5T and 3.0T data from each subject into SRI24 coordinates via that subject's 3.0T SPGR image (rather than separately via the early-echo EPSE

images at each field strength) ensures that the unavoidable inter-subject registration imperfections are consistent for images from both field strengths.

The 1.5T SWI magnitude images were rigidly registered to a simultaneously acquired structural SPGR image, which was then registered nonrigidly to the same subject's 3.0T SPGR image. The SWI-SPGR registration was limited to a rigid transformation because signal dropouts in magnitude SWI due to B0 field inhomogeneities prevented nonrigid correction of the relatively small distortions between SWI and SPGR. Again, via concatenation of transformations, the phase images were reformatted into SRI24 space, again with a 5-pixel radius cosine sinc kernel. All data were analyzed in common 1-mm isotropic SRI24 atlas space.

Region of interest identification

Voxel-by-voxel FDRI images (FDRI=($R2_{3T} - R2_{1.5T}$)/1.5T) were created for each subject and used to make a group FDRI average, comprising all young and elderly subjects. A similar group average was made for the phase images, and separate young and elderly group averages were made for display purposes (Figure 1).

Bilateral caudate, globus pallidus, putamen, thalamus, and white matter sample regions of interest (ROI) were drawn (by A.P.) on the group-average (all young plus all old subjects) FDRI images in common SRI24 space, reformatted in the *coronal* plane (Pfefferbaum et al., 2009). The globus pallidus, putamen, caudate, and white matter sample were drawn on 10 contiguous, 1-mm thick slices at an anterior-posterior location that maximized the presence of all three basal ganglia structures in the same slices. The thalamus was drawn on the next 10 contiguous slices posterior to the basal ganglia. The caudate was eroded one pixel and thalamus was eroded two pixels on a slice-by-slice basis to avoid partial voluming of CSF. Substantia nigra and red nucleus ROIs were also identified, based on their FDRI intensities (Figure 2).

For each subject and for each ROI at each field strength, the mean intensity of all voxels in an ROI for the early- and late-echo EPSE were used to compute $R2_{3T}$ and $R2_{1.5T}$ and the FDRI [($R2_{3T} - R2_{1.5T}$)/1.5T]. SWI phase was computed as the phase in radians for all voxels identified in each ROI.

The same ROIs (caudate, globus pallidus, putamen, thalamus, white matter sample, substantia nigra, and red nucleus) were manually identified on the group-average SWI data (all young and all elderly combined), reformatted in the *axial* plane (Ogg et al., 1999), and guided by phase conspicuity. When drawing ROIs on the SWI data, attempt was made to exclude the bright rims around the globus pallidus and putamen as well as the division between them. Although this approach biases the data towards more negative phase values, it was done to maximize the sensitivity of SWI to age effects. SWI phase was computed in radians for all voxels identified on the group-average phase images, and FDRI was computed as above on these ROIs.

Thus, both FDRI intensity and SWI conspicuity were each used to guide ROI delineation, and FDRI and SWI were computed for both ROI approaches. Across the ROIs, FDRI ranged from 0.107 s^{-1}/Tesla to 6.094 s^{-1}/Tesla, and SWI phase ranged from −.480 to +.874 radians.

Statistical analysis

Two-group (young vs. elderly) by two-hemisphere (left vs. right) repeated-measures analyses of variance (ANOVA) were conducted for each of the seven bilateral brain regions (globus pallidus, putamen, caudate nucleus, thalamus, red nuclei, substantia nigra, and the white matter sample) and each iron metric (FDRI and SWI) separately to test for group-by-hemisphere effects. We did not expect group-by-hemisphere interactions, that is, we predicted that in regions showing an age effect both hemispheres would be similarly affected by age. Taken

from published results, we used a series of two group-by-two ROI ANOVAs to test the primary hypothesis that both the globus pallidus and putamen would be high in iron concentration, but that the putamen would have disproportionately more iron in the elderly than young group, i.e., the group-by-ROI interaction would be significant. Additional group differences for each ROI were examined with t-tests. Comparisons of the two iron indices with each other and also with published postmortem values were based on nonparametric (Spearman) correlations.

Results

All ROI and statistical analyses were conducted twice, once on the FDRI-identified ROIs and again on the SWI-identified ROIs. Higher FDRI and lower SWI values indicate greater presence of iron; thus, we tested the hypotheses that, relative to the young group, the elderly group would have higher FDRI and lower SWI in striatal and brain stem ROIs, but not in thalamic or white matter ROIs. We also predicted that the ROI iron values would correlate with published postmortem iron values (Hallgren and Sourander, 1958), with positive correlations with FDRI and negative ones with SWI.

Group differences and ROI profiles: ANOVAs and t-tests

A series of group-by-hemisphere ANOVAs tested for differential laterality effects in the young and elderly groups that would be supported by significant interactions. No consistent asymmetries favoring one or the other group were identified; for only one interaction (substantia nigra) was the p-value less than .05 (p=.0255). Thus, all subsequent analyses were based on bilateral data, expressed as the mean of the left and right measures for each ROI and are presented in Table 1. Two Hanning filter kernel sizes were used to calculate SWI data and the results from each filter appear in Table 1, the figures, and the statistical analyses below.

The a priori hypothesis was that the globus pallidus would have higher concentration of iron than putamen irrespective of age, but that the elderly group would have disproportionately greater iron than the young in the putamen. Thus, we expected age group-by-ROI interaction for iron concentration in these two structures.

FDRI-based ROIs (Table 1a)

FDRI—In support of our hypothesis, the group-by-ROI (globus pallidus vs. putamen) ANOVA yielded a significant interaction (F(1,21)=4.794, p=.04) (Figure 3, top left). Follow-up t-tests revealed that the elderly group had significantly higher FDRI (that is, evidence for more iron) than the young group in the putamen (t(21)=4.150, p=.0005) and showed a trend in the same direction for the globus pallidus (t(21)=1.942, p=.0656).

Group comparison for the remaining ROIs revealed that the FDRI values in striatal and brain stem ROIs were higher in the elderly than young group, indicative of higher iron concentration, and also for the red nucleus (t(21)=2.507, p=.0205) and showed a trend in the substantia nigra (t(21)=2.033, p=.0549). Although FDRI was higher in the caudate of the elderly than the young, the difference was not significant (t(21)=1.317, p=.202). By contrast, the FDRI values in the thalamic (t(21)=2.070, p=.0509) and white matter (t(21)=1.868, p=.0758) samples tended to be lower (indicative of less iron) in the elderly than the young group.

SWI—Lower SWI values are indicative of higher local iron concentration. The group-by-ROI (globus pallidus vs. putamen) ANOVA yielded significant interactions for both filter sizes: the 64-pixel size kernel (F(1,21)=3.067, p=.0001) and the 96-pixel size kernel (F(1,21)=21.368, p=.0001). Using t-tests, compared with the young group, the elderly group had evidence of greater iron (i.e., lower SWI values) in the putamen (64 kernel t(21)=3.987, p=.0007; 96 kernel t(21)=4.591, p=.0002) and the globus pallidus (64 kernel t(21)=3.067, p=.0059; 96 kernel t(21)

=2.319, p=.0306). Although the group differences were significant for both regions (Figure 3, top right), the ANOVA interaction was due to the fact that the globus pallidus measure indicated significantly *less* iron in the elderly than the young group, and the mean phase was positive for both groups and for both kernel sizes. The remaining ROIs showed no significant age differences regardless of filter size.

SWI-based ROIs (Table 1b)

FDRI—The pattern of mean group differences was the same as for the values derived from FDRI-based ROIs, with the only difference being in the robustness of the age effect, which varied by ROI. The group-by-ROI (globus pallidus vs. putamen) ANOVA yielded a significant interaction (F(1,21)=13.191, p=.0016) (Figure 3, bottom left). Further, the higher FDRI in the elderly than young group was significant in the caudate (t(21)=2.186, p=.0403) and putamen (t(21)=3.718, p=.0013) with a trend in the substantia nigra (t(21)=1.720, p=.1001). The expected opposite effect, with lower FDRI in the elderly than young group, occurred in the thalamus (t(21)=2.636, p=.0154) and white matter sample (t(21)=2.906, p=.0085).

SWI—The group-by-ROI (globus pallidus vs. putamen) interactions were significant for both filter sizes: the 64-pixel size kernel (F(1,21)=7.1744, p=.0141) and the 96-pixel size kernel (F (1,21)=5.882, p=.0244) (Figure 3, bottom right). The SWI values were indicative of significantly more iron in the putamen (64 kernel t(21)=4.249, p=.0004; 96 kernel t(21)=4.88, p=.0001) but not globus pallidus (64 kernel t(21)=.510, p=.616; 96 kernel t(21)=.717, p=.481) of the elderly than the young group. The caudate also showed significantly more iron in the elderly than young for the 96 kernel (t(21)=2.609, p=.0164) but not the 64 kernel filter (t(21) =.924, p=.366).

The red nucleus is a small structure and radiologically heterogeneous, appearing as a bright center and dark peripheral, densely vascularized component (Duvernoy) on phase SWI (Manova et al., 2009). In acknowledgment of the differential effect such sharp signal differences can have on phase, we divided the red nucleus into a center and a peripheral capsule and calculated phase in each section. The central portion of the red nucleus was a 5 mm^2 in-plane sample in the center of the structure from the SWI-based ROIs and comprised approximately 25% of the volume of the red nucleus, with the remaining 75% designated as the capsule. Both kernel size analyses yielded the same pattern of results: SWI phase was higher, indicative of *less* iron, in the center of the elderly than young (64 kernel t(21)=2.663, p=.0146; 96 kernel t(21)=2.502, p=.0207); by contrast, the young and elderly groups did not differ from each other in phase-detected iron in the capsule of the red nucleus (64 kernel t(21) =.637, p=.531; 96 kernel t(21)=.941, p=.358).

Within and across FDRI and SWI values by ROI

To examine the consistency between iron estimates, we correlated the FDRI values derived from coronal images with SWI values derived from axial images (based on the 64 and 96 kernel filters separately) of the 23 subjects for each ROI and expected the correlations to be negative. Regions with the highest iron content showed the highest negative correlations, which improved with the kernel filter size. Specifically, the only correlations to reach the p=.05 level of significance involved iron estimates in the globus pallidus (64-kernel ROI r=−.43, p=.0438; 96-kernel ROI r=−.56, p=.0086) and putamen (64-kernel ROI r=−.45, p=.0338; 96-kernel ROI r=−.53, p=.0122).

Using ANOVA, the mean FDRI values across the 23 subjects produced significant differences in iron concentration across the three basal ganglia structures (globus pallidus > putamen > caudate, F(2,44)=265.05, p=.0001), whereas the phase measurement produced no significant difference among these three structures (F(2,44)=.854, p=.4326).

Correlations of FDRI and SWI values with postmortem iron concentrations

Figure 4 presents the mean±SD iron concentration determined postmortem in each ROI (Hallgren and Sourander, 1958) on the X-axis and the mean±SD FDRI from FDRI-based ROIs and SWI phase in radians from SWI-based ROIs in young plus elderly subjects on the Y-axis. The relationship between the postmortem and in vivo FDRI data is virtually perfectly ranked in order of magnitude (Rho=1.0, p=.0143), whereas the rankings between the postmortem and in vivo SWI data were less than perfect but higher for the correlations based on the 96-pixel kernel (Rho=−.82, p=.0442) than the 64-pixel kernel (Rho=−.43, p=.29).

Discussion

The accumulation of iron in the brain with advancing age can have significant effects on motor and cognitive function (Bartzokis et al., 2008; Sullivan et al., 2009). The current study was undertaken to examine the benefits and limitations of two currently used in vivo methods for brain iron quantification—FDRI and SWI—with a direct comparison of the two different methods in a within-subject design in healthy young compared with elderly men and women. We delineated regions of interest based on the group average of all subjects for each method and assessed the data with both methods: The FDRI regions of interest were based on our previous study of normal aging (Pfefferbaum et al., 2009) and used a coronal slice orientation for delineation; for SWI we used an axial presentation, following the mainstay of published studies using the phase shift method (Haacke et al., 2009). Although this approach used the dependent variable to define itself, it afforded the greatest chance of demonstrating signal properties reflecting brain iron.

Non-heme brain iron in sufficient concentration to affect MR contrast resides in ferritin or hemosiderin molecules (Schenck, 2003), which increase R2 and R2* (relaxivity). R2* effects can be assessed by measuring R2* directly (Duyn et al., 2007), R2' (R2* – R2) (Gelman et al., 1999; Graham et al., 2000), or through the effects on phase (Haacke et al., 2009; Ogg et al., 1999; Yao et al., 2009). Both phase and R2 are affected by heme iron, i.e. deoxygenated hemoglobin (Duyn et al., 2007), although phase much more so than R2. Deoxygenated hemoglobin is less paramagnetic than oxygenated hemoglobin and influences phase, especially as seen in vasculature. As noted by Duyn and colleagues (Duyn et al., 2007), phase contrast observed in gradient-recalled echo images of the cortex could be caused by the relatively greater blood volume in gray matter than white matter as well as by differences in ferritin content. Additional gray matter/white matter phase contrast could be due to greater cholesterol-like lipid content in myelin-rich white matter (cf., Duyn et al., 2007). Finally, phase effects can be influenced by the geometric orientation of the structure relative to the magnetic field (Duyn et al., 2007) and air/bone/tissue interfaces.

The water content of the tissue under examination may influence the R2-based measurement approach. There is generally a decrease in R2 with advancing age in white matter and thalamus but little age-related difference in striatal gray matter structures (Agartz et al., 1991; Breger et al., 1991; Pfefferbaum et al., 2009; Siemonsen et al., 2008). By contrast, age-related R2* decrease is prominent in the striatum (Siemonsen et al., 2008). The age-related decrease in R2 readily observed in white matter is presumably from increased interstitial fluid with an extreme condition being leukoaraiosis. In fact there is evidence for age-related increased mean diffusivity in both white matter and gray matter structurally, notably, the globus pallidus (Pfefferbaum et al., 2009). If there is similar increase in interstitial fluid in the striatum, any decrease in R2 could be counteracted by an increase in R2 caused by iron presence. Conversely, age-related decrease in R2 would serve to cancel, to some extent, the R2 lengthening effect of iron at a given field strength, but this effect would be somewhat mitigated by the FDRI approach, which relies on a differential R2 effect across field strengths.

Both FDRI and SWI successfully detected the high concentration of iron in the globus pallidus regardless of age and the significantly greater presence of iron in the putamen with advancing age. Compared with FDRI, however, SWI was less sensitive in other regions of the brain, perhaps because iron deposition is not the only contribution to susceptibility-induced phase effects, whereas a substantial influence of signal differences between field strengths is attributable to iron concentration. Further, perhaps due to its higher spatial resolution, SWI is more sensitive to subtle signal changes within a region than FDRI. For instance, the red nucleus is highly visible, but there are variations in the SWI signal even in this small structure. Thus, measurement of phase in the center of the red nucleus yielded different age effects from those observed in the capsule, which more closely comported with in vivo FDRI results and published postmortem values than did the center (Duvernoy, 1999).

When examining multiple regions of interest across the brain, it is clear that FDRI and SWI do not measure the same tissue characteristics. In some parts of some structures, such as the globus pallidus, negative phase was prominent, suggesting significant iron accumulation; however, this phenomenon appeared in only part of the anatomical boundaries of the structure. The putamen, residing just lateral to the globus pallidus, also showed significant signal heterogeneity, with much less negative phase, if not positive phase, relative to the globus pallidus. Although SWI's sensitivity to heterogeneity may well be a strength in high-resolution detection of tissue differences, especially at high field strengths (e.g., at 7T; Duyn et al., 2007), this heightened capability may be a liability when quantifying a single source of susceptibility, such as iron.

Adjustment of filter kernel size in determining phase for SWI, as prescribed by Haacke and colleagues (Haacke et al., 2009; Haacke et al., 2004; Wang et al., 2000), changed the sensitivity of the measure to detect iron. Filter kernel size has a different impact on structures of different size and on the ability to remove artifact due to air/tissue interface, especially in frontal brain regions as they affect the phase observed in the caudate nucleus. Specifically, application of a 64-pixel kernel yielded a higher estimate of iron in the putamen of elderly relative to young adults, and a 96-pixel kernel solution provided similar age effects. A caveat, however, is that phase was sensitive to the age-related differential detection of iron in regions measured on axial slices, the plane of SWI acquisition used herein and in the mainstay of published studies using the phase shift method, but iron measured on reconstructed coronal images only inconsistently comported with results based on axial measures. In contrast with this SWI restriction, iron measured with FDRI was little affected by plane of measurement with respect to plane of acquisition. This lack of robustness to plane of iron measurement relative to plane of data acquisition is likely influenced by the heterogeneity of phase within structures.

The data reported here were collected on normal volunteers who did not present with complaints of brain pathology, and the data are meant to be an exposition of “normal aging” effects. The greater presence of iron detected with SWI phase in the putamen of elderly compared with young adults comports with the prominent age effect reported by Xu et al. (Xu et al., 2008). Unlike Xu et al. who reported higher iron levels in the left than right hemisphere, the age and iron effects we observed were bilateral. The sensitivity of the two iron measurement techniques to pathology might be quite different. SWI, especially with high spatial resolution, might be very sensitive to hemosiderin from small infarcts (Mittal et al., 2009) that are undetected by FDRI. Indeed, SWI phase measures are exquisitely sensitive to both heme and non-heme iron and other tissue properties, such as membranes relatively rich in vasculature and junctions between tissue compartments. The non-iron sources of phase effects, however, confound its use as a global survey measure of age-dependent acceleration of brain iron deposition. Nonetheless, SWI could be useful in longitudinal study, where brain changes are assessed on a within-subject basis.

The aging effects, which we have previously demonstrated in a study based on legacy data acquired with sequences less optimal for iron detection and quantification (Pfefferbaum et al., 2009), were replicated herein with new FDRI measures, including the readily visualized increase in FDRI signal in the putamen in the older subjects (also see Bartzokis et al., 2007a). This age effect was also demonstrated with SWI. A further source of convergent validity of the FDRI measure was its high correlation with the published postmortem data on regional brain iron (Hallgren and Sourander, 1958). Although improved with a larger kernel size filter, the regional SWI correlation with postmortem data did not reach the level achieved with the FDRI measures, and the lack of distinction across the basal ganglia structures calls into question the generalized use of this method across the brain for iron quantification.

We conclude that, for quantifying brain iron concentration, advantages of SWI include the need for only one field strength scanner and the ability to achieve high spatial resolution in much shorter acquisition time (12 min) than FDRI (45 min). Advantages of FDRI include its greater specificity than SWI for detection of non-heme iron as based on correlation with postmortem data across multiple iron-rich brain structures. The limitations of the SWI iron approach in the current data set do not appear to be attributable to inadequate accuracy from low SNR, which could be improved by acquiring data at higher field strengths, but rather the lack of phase uniformity across a given structure. To the extent that SWI measures iron, SWI may be adequate for detecting age-related differences in iron concentration in some structures or some parts of a structure. By contrast, for multiple structure analysis and whole structure quantification of iron, FDRI is preferred.

Acknowledgment

We thank Melanie Atmadja and Mallika Bhandarkar, our research assistants who recruited and scheduled the subjects and performed much of the MRI data acquisition. This work was supported by NIH grants AG017919, AA005965, AA017168.

References

Agartz I, Saaf J, Wahlund LO, Wetterberg L. T1 and T2 relaxation time estimates in the normal human brain. Radiology 1991;181:537–543. [PubMed: 1924801]

Bartzokis G, Aravagiri M, Oldendorf WH, Mintz J, Marder SR. Field dependent transverse relaxation rate increase may be a specific measure of tissue iron stores. Magnetic Resonance in Medicine 1993;29:459–464. [PubMed: 8464361]

Bartzokis G, Lu PH, Tingus K, Mendez MF, Richard A, Peters DG, Oluwadara B, Barrall KA, Finn JP, Villablanca P, Thompson PM, Mintz J. Lifespan trajectory of myelin integrity and maximum motor speed. Neurobiol Aging Oct. 2008Epub ahead of print

Bartzokis G, Lu PH, Tishler TA, Fong SM, Oluwadara B, Finn JP, Huang D, Bordelon Y, Mintz J, Perlman S. Myelin breakdown and iron changes in Huntington's disease: pathogenesis and treatment implications. Neurochemical Research 2007a;32:1655–1664. [PubMed: 17484051]

Bartzokis G, Mintz J, Sultzer D, Marx P, Herzberg JS, Phelan CK, Marder SR. In vivo MR evaluation of age-related increases in brain iron. American Journal of Neuroradiology 1994;15:1129–1138. [PubMed: 8073983]

Bartzokis G, Tishler TA, Lu PH, Villablanca P, Altshuler LL, Carter M, Huang D, Edwards N, Mintz J. Brain ferritin iron may influence age- and gender-related risks of neurodegeneration. Neurobiology of Aging 2007b;28:414–423. [PubMed: 16563566]

Bizzi A, Brooks RA, Brunetti A, Hill JM, Alger JR, Miletich RS, Francavilla TL, Di Chiro G. Role of iron and ferritin in MR imaging of the brain: a study in primates at different field strengths. Radiology 1990;177:59–65. [PubMed: 2399339]

Brass SD, Chen NK, Mulkern RV, Bakshi R. Magnetic resonance imaging of iron deposition in neurological disorders. Top Magn Reson Imaging 2006;17:31–40. [PubMed: 17179895]

Breger RK, Yetkin FZ, Fischer ME, Papke RA, Haughton VM, Rimm AA. T1 and T2 in the cerebrum - Correlation with age, gender, and demographic factors. Radiology 1991;181:545–547. [PubMed: 1924802]

Duvernoy HM. Human Brain Stem. 1999

Duyn JH, van Gelderen P, Li TQ, de Zwart JA, Koretsky AP, Fukunaga M. High-field MRI of brain cortical substructure based on signal phase. Proc Natl Acad Sci U S A 2007;104:11796–11801. [PubMed: 17586684]

Gelman N, Gorell JM, Barker PB, Savage RM, Spickler EM, Windham JP, Knight RA. MR imaging of human brain at 3.0 T: preliminary report on transverse relaxation rates and relation to estimated iron content. Radiology 1999;210:759–767. [PubMed: 10207479]

Graham JM, Paley MN, Grunewald RA, Hoggard N, Griffiths PD. Brain iron deposition in Parkinson's disease imaged using the PRIME magnetic resonance sequence. Brain 2000;123(Pt 12):2423–2431. [PubMed: 11099445]

Haacke EM, Ayaz M, Khan A, Manova ES, Krishnamurthy B, Gollapalli L, Ciulla C, Kim I, Petersen F, Kirsch W. Establishing a baseline phase behavior in magnetic resonance imaging to determine normal vs. abnormal iron content in the brain. J Magn Reson Imaging 2007;26:256–264. [PubMed: 17654738]

Haacke EM, Cheng NY, House MJ, Liu Q, Neelavalli J, Ogg RJ, Khan A, Ayaz M, Kirsch W, Obenaus A. Imaging iron stores in the brain using magnetic resonance imaging. Magnetic Resonance Imaging 2005;23:1–25. [PubMed: 15733784]

Haacke EM, Mittal S, Wu Z, Neelavalli J, Cheng YC. Susceptibility-weighted imaging: technical aspects and clinical applications, part 1. AJNR Am J Neuroradiol 2009;30:19–30. [PubMed: 19039041]

Haacke EM, Xu Y, Cheng YC, Reichenbach JR. Susceptibility weighted imaging (SWI). Magn Reson Med 2004;52:612–618. [PubMed: 15334582]

Hallgren B, Sourander P. The effect of age on the non-haemin iron in the human brain. J Neurochem 1958;3:41–51. [PubMed: 13611557]

Jenkinson M. A fast, automated, N-dimensional phase unwrapping algorithm. Magnetic Resonance in Medicine 2003;49:193–197. [PubMed: 12509838]

Manova ES, Habib CA, Boikov AS, Ayaz M, Khan A, Kirsch WM, Kido DK, Haacke EM. Characterizing the Mesencephalon Using Susceptibility-Weighted Imaging. AJNR Am J Neuroradiol. 2009

Mattis, S. Dementia Rating Scale (DRS) Professional Manual. Psychological Assessment Resources, Inc.; Odessa, FL: 1988.

Mittal S, Wu Z, Neelavalli J, Haacke EM. Susceptibility-weighted imaging: technical aspects and clinical applications, part 2. AJNR Am J Neuroradiol 2009;30:232–252. [PubMed: 19131406]

Ogg RJ, Langston JW, Haacke EM, Steen RG, Taylor JS. The correlation between phase shifts in gradient-echo MR images and regional brain iron concentration. Magn Reson Imaging 1999;17:1141–1148. [PubMed: 10499676]

Pfefferbaum A, Adalsteinsson E, Rohlfing T, Sullivan EV. Diffusion tensor imaging of deep gray matter brain structures: Effects of age and iron concentration. Neurobiology of Aging. 2009on line May28

Rohlfing T, Maurer CR. Nonrigid image registration in shared-memory multiprocessor environments with application to brains, breasts, and bees. IEEE Transactions on Information Technology in Biomedicine 2003;7:16–25. [PubMed: 12670015]

Rohlfing T, Zahr NM, Sullivan EV, Pfefferbaum A. The SRI24 multi-channel brain atlas: Construction and applications Medical Imaging 2008: Image Processing. Proceedings of SPIE 2008;6914:691409.

Schenck JF. Magnetic resonance imaging of brain iron. J Neurol Sci 2003;207:99–102. [PubMed: 12614939]

Siemonsen S, Finsterbusch J, Matschke J, Lorenzen A, Ding XQ, Fiehler J. Age-dependent normal values of T2* and T2' in brain parenchyma. AJNR Am J Neuroradiol 2008;29:950–955. [PubMed: 18272561]

Sullivan EV, Adalsteinsson E, Rohlfing T, Pfefferbaum A. Relevance of iron deposition in deep gray matter brain structures to performance on cognitive and motor tests in healthy elderly men and women: Exploratory findings. Brain Imaging and Behavior. 2009In press

Wang Y, Yu Y, Li D, Bae KT, Brown JJ, Lin W, Haacke EM. Artery and vein separation using susceptibility-dependent phase in contrast-enhanced MRA. J Magn Reson Imaging 2000;12:661–670. [PubMed: 11050635]

Xu X, Wang Q, Zhang M. Age, gender, and hemispheric differences in iron deposition in the human brain: an in vivo MRI study. Neuroimage 2008;40:35–42. [PubMed: 18180169]

Yao B, Li TQ, Gelderen P, Shmueli K, de Zwart JA, Duyn JH. Susceptibility contrast in high field MRI of human brain as a function of tissue iron content. Neuroimage 2009;44:1259–1266. [PubMed: 19027861]

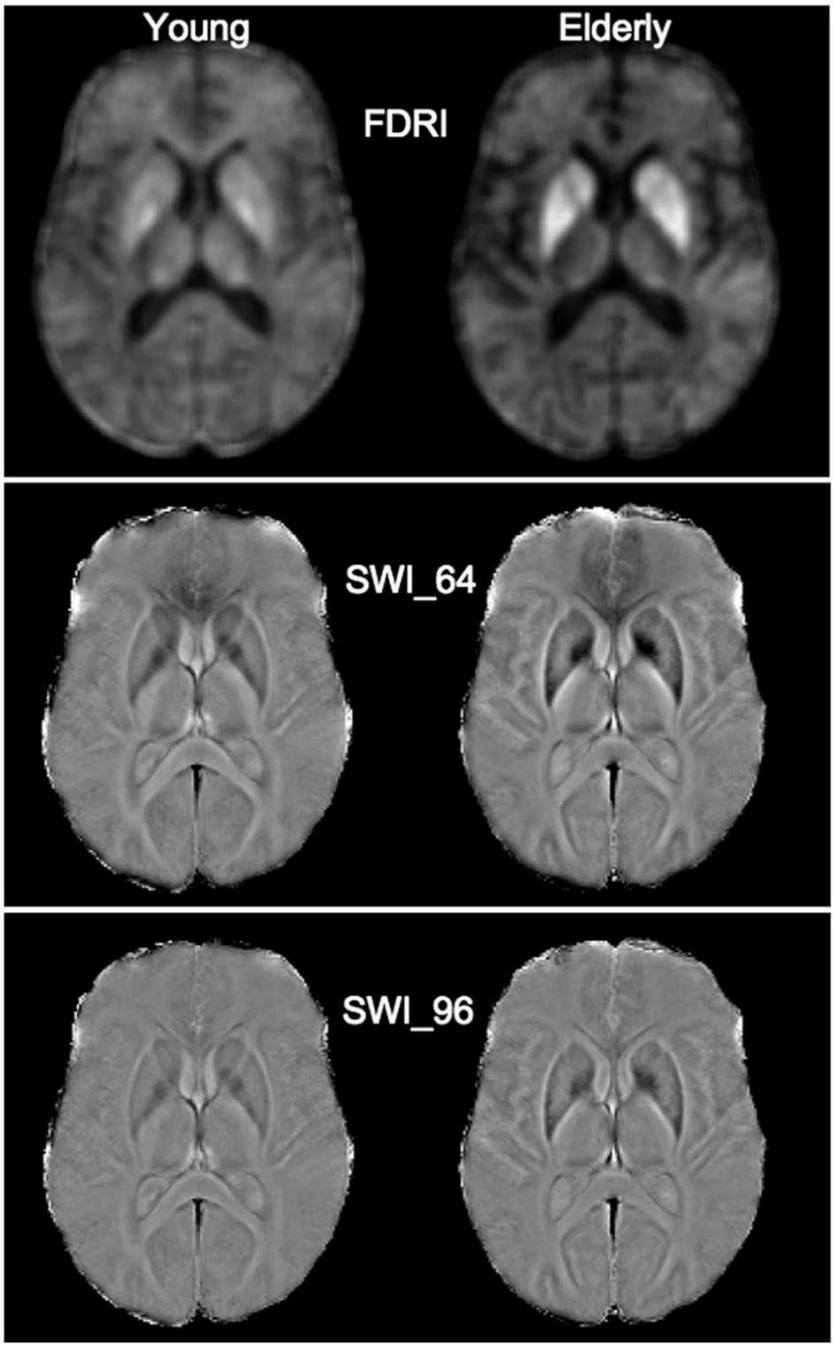

Figure 1.
Young (left) and elderly (right) group averages for FDRI images (top) and SWI images with 64-pixel kernel (middle) and 96-pixel kernel Hanning filters (bottom). Greater iron concentration yields higher (brighter) FDRI signal but lower (darker) SWI phase signal.

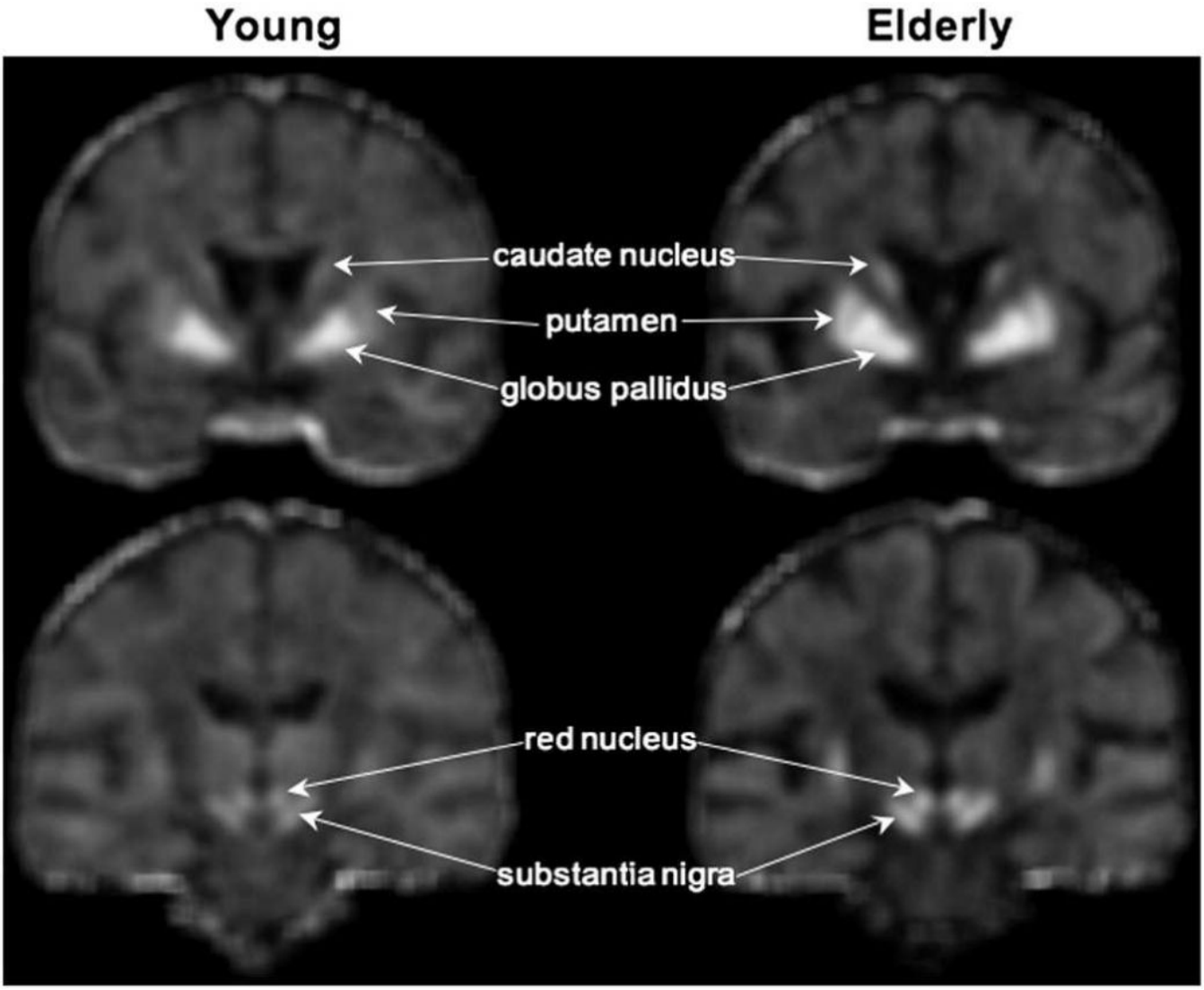

Figure 2.
Examples of FDRI conspicuity for three striatal and two brain stem regions for young (left) and elderly (right) groups.

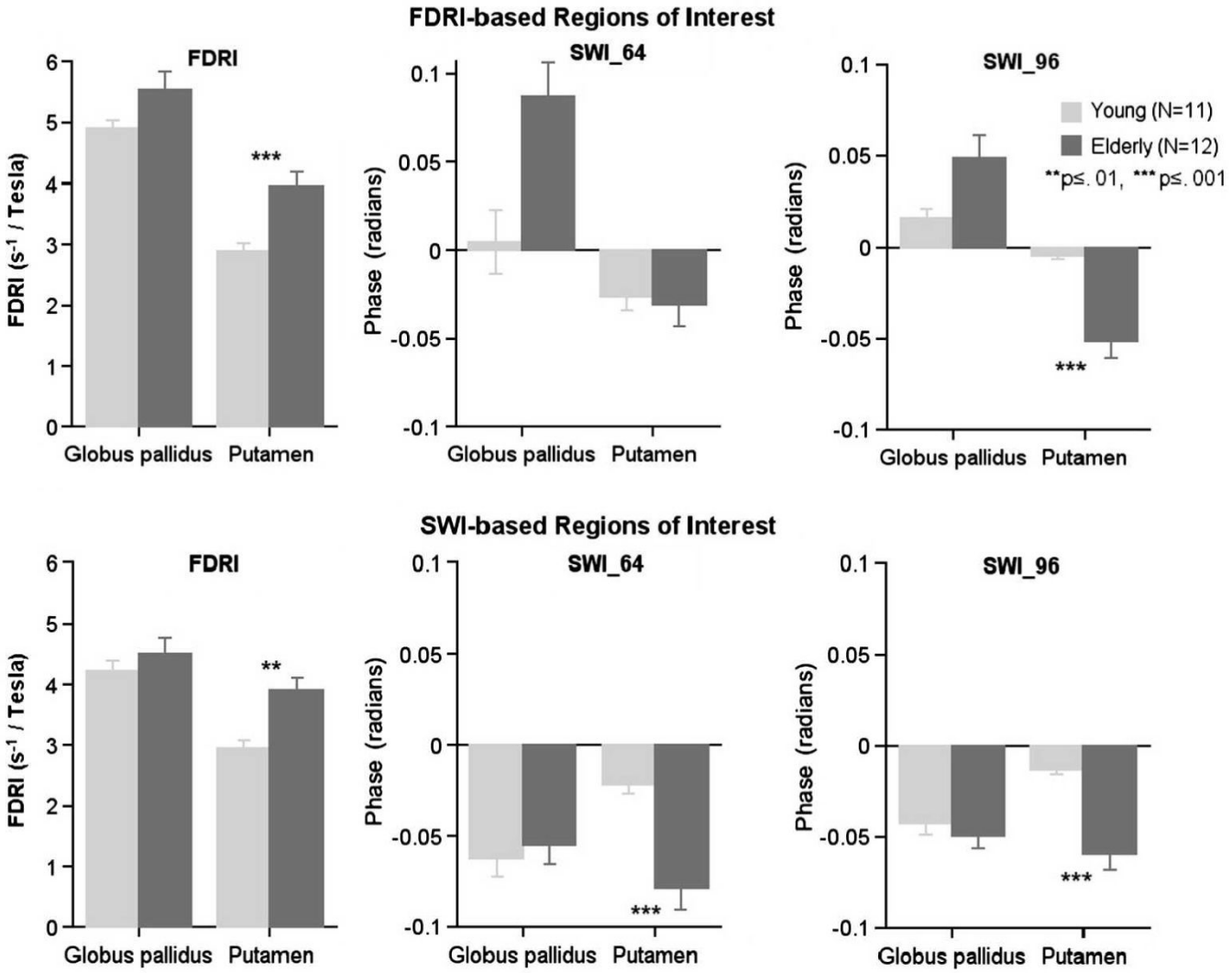

Figure 3.

Top: Iron values obtained from FDRI-based ROIs (left) and SWI-based ROIs with the 64-pixel kernel (middle) and 96-pixel kernel (right): Mean±SE FDRI in s^{-1}/Tesla (left) and SWI phase in radians (middle and right) of the globus pallidus and putamen in young and elderly groups. Bottom: Iron values obtained from SWI-based (axial) ROIs.

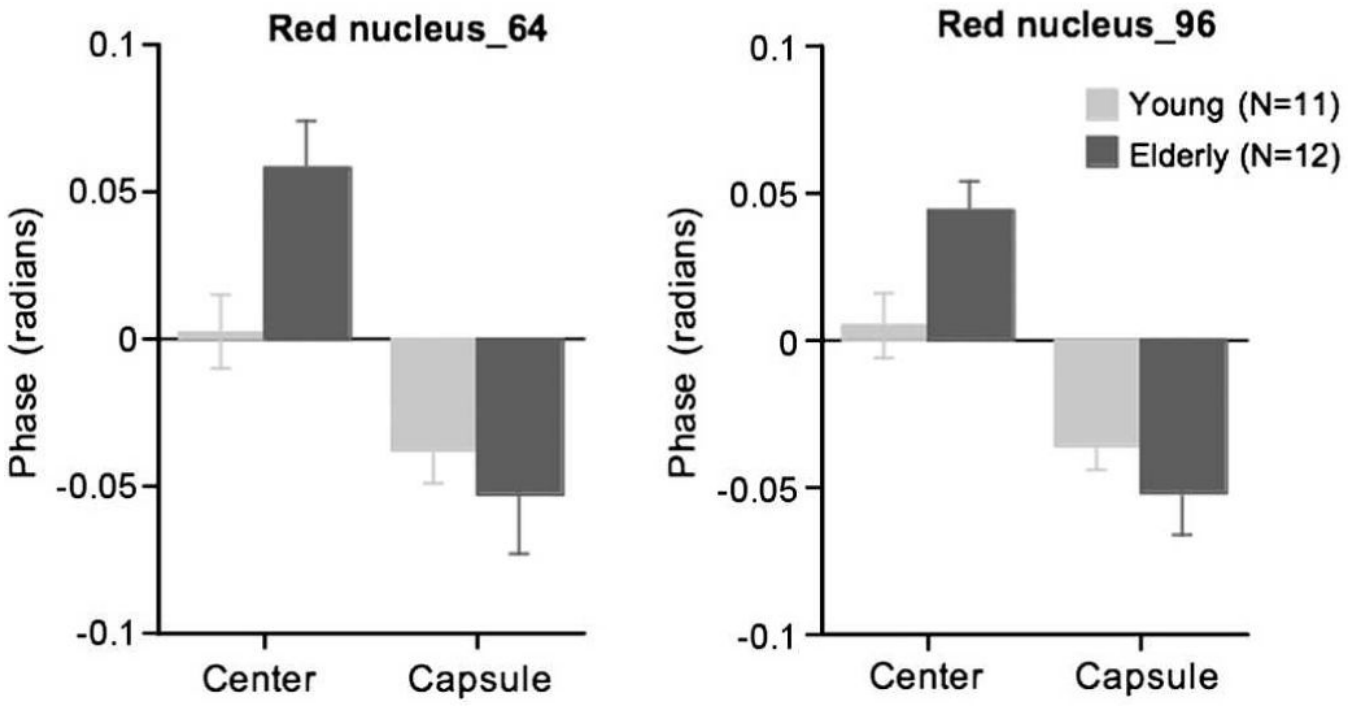

Figure 4.
Mean±SE SWI phase in radians (left for the 64-pixel kernel and right for the 96-pixel kernel) of the center and capsule of the red nucleus in young and elderly groups.

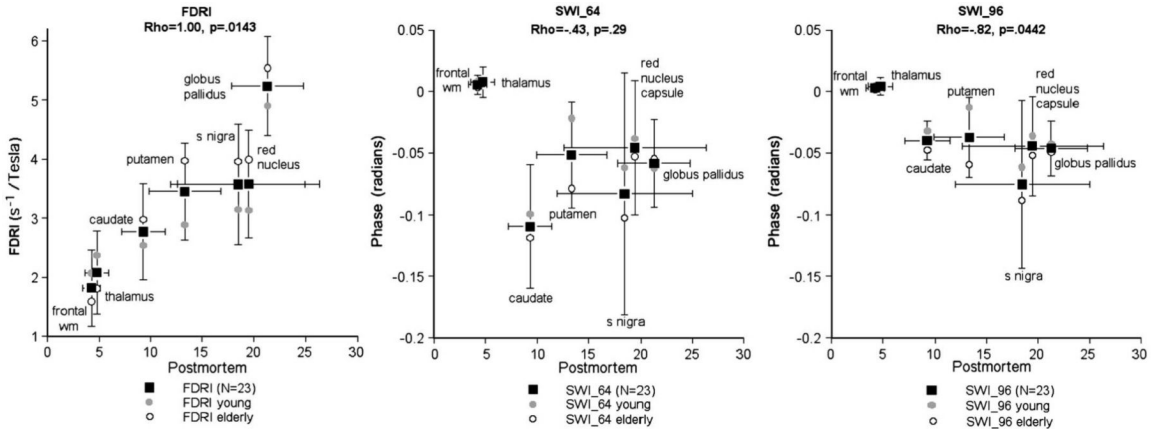

Figure 5.

X-axis: Mean±SD iron concentration (mg/100g fresh weight) determined postmortem in each ROI (Hallgren and Sourander, 1958). Y-axis: Mean±SD FDRI in s^{-1}/Tesla (left) from FDRI-based ROIs and SWI phase in radians (middle and right) from SWI-based ROIs in young plus elderly subjects; the gray circles indicate the mean of the young group, and the open circles indicate the mean of the elderly group.

Table 1a

Mean (±SD) iron measure in each coronal region for FDRI and SWI; t-tests (df=21) compare young vs. elderly groups

Region	FDRI				SWI_64				SWI_96			
	Young (N=11)	Elderly (N=12)			Young (N=11)	Elderly (N=12)			Young (N=11)	Elderly (N=12)		
	2.070	1.592	t=	1.867	0.004	−0.004	t=	1.225	0.004	0.001	t=	1.735
Frontal WM	(0.612)	(0.614)	p=	.076	(0.014)	(0.011)	p=	.234	(0.004)	(0.006)	p=	.097
	2.375	1.810	t=	2.071	0.004	0.007	t=	0.692	0.001	0.001	t=	0.312
Thalamus	(0.637)	(0.667)	p=	.051	(0.014)	(0.007)	p=	.496	(0.009)	(0.004)	p=	.758
	2.542	2.983	t=	1.316	−0.026	−0.031	t=	0.299	−0.011	−0.010	t=	0.157
Caudate	(0.388)	(1.045)	p=	.202	(0.026)	(0.044)	p=	.767	(0.016)	(0.026)	p=	.876
	2.893	3.971	t=	**4.150**	0.000	−0.064	t=	**3.987**	−0.004	−0.051	t=	**4.591**
Putamen	(0.414)	(0.764)	p=	**.001**	(0.012)	(0.052)	p=	**.001**	(0.006)	(0.033)	p=	**.000**
	4.898	5.540	t=	1.942	0.005	0.087	t=	3.066†	0.016	0.049	t=	2.318†
Globus pallidus	(0.436)	(1.012)	p=	.066	(0.060)	(0.068)	p=	.005	(0.018)	(0.043)	p=	.031
	3.148	3.961	t=	2.032	0.045	0.072	t=	0.695	0.022	0.047	t=	0.976
S nigra	(0.954)	(0.961)	p=	.055	(0.052)	(0.117)	p=	.494	(0.032)	(0.082)	p=	.340
	3.131	3.990	t=	**2.507**	0.001	0.051	t=	3.092†	−0.009	0.019	t=	2.258†
Red nucleus	(0.879)	(0.763)	p=	**.021**	(0.030)	(0.045)	p=	.005	(0.022)	(0.035)	p=	.034

Numbers in bold indicate significant differences.

† Group difference is in the unexpected direction, with elderly having less iron than young.

Table 1b

Mean (±SD) iron measure in each axial region for FDRI and SWI

Region	FDRI				SWI_64				SWI_96			
	Young (N=11)	Elderly (N=12)			Young (N=11)	Elderly (N=12)			Young (N=11)	Elderly (N=12)		
	2.025	1.543	t=	**2.905**	0.008	0.003	t=	1.540	0.004	0.002	t=	1.481
Frontal WM	(0.332)	(0.448)	p=	**.009**	(0.006)	(0.008)	p=	.138	(0.003)	(0.005)	p=	.153
	2.328	1.703	t=	**2.636**	0.009	0.007	t=	0.412	0.004	0.004	t=	0.001
Thalamus	(0.513)	(0.611)	p=	**.015**	(0.014)	(0.011)	p=	.684	(0.008)	(0.007)	p=	.998
	2.535	3.201	t=	**2.186**	−0.100	−0.119	t=	0.923	−0.032	−0.047	t=	**2.609**
Caudate	(0.480)	(0.900)	p=	**.040**	(0.065)	(0.032)	p=	.366	(0.015)	(0.013)	p=	**.016**
	2.953	3.900	t=	**3.718**	−0.022	−0.079	t=	**4.249**	−0.013	−0.059	t=	**4.883**
Putamen	(0.421)	(0.742)	p=	**.001**	(0.018)	(0.041)	p=	**.000**	(0.009)	(0.030)	p=	**.000**
	3.229	3.421	t=	0.469	−0.062	−0.103	t=	0.990	−0.061	−0.088	t=	0.942
S nigra	(0.954)	(1.003)	p=	.643	(0.122)	(0.071)	p=	.333	(0.086)	(0.047)	p=	.356
	4.230	4.502	t=	0.856	−0.062	−0.055	t=	0.509	−0.043	−0.049	t=	0.716
Globus pallidus	(0.518)	(0.928)	p=	.401	(0.035)	(0.037)	p=	.615	(0.021)	(0.024)	p=	.481
	3.273	3.933	t=	1.720	–	–	–	–	–	–		–
Red nucleus[§]	(0.982)	(0.858)	p=	.100	–	–	–	–	–	–		–
	–	–		–	0.0028	0.058	t=	2.662[†]	0.006	0.044	t=	2.502[†]
center	–	–		–	(0.041)	(0.056)	p=	.014	(0.037)	(0.036)	p=	.021
	–	–		–	−0.038	−0.053	t=	0.637	−0.036	−0.052	t=	0.94
capsule	–	–		–	(0.037)	(0.068)	p=	.530	(0.027)	(0.049)	p=	.357

Numbers in bold indicate significant differences.

[†] Group difference is in the unexpected direction, with elderly having less iron than young.

[§] The red nucleus was divided into the center and capsule on the axial images for SWI only.